RSC Advances

PAPER

View Article Online
View Journal | View Issue

Cite this: *RSC Adv.*, 2021, **11**, 10235

Nanorod bundle-like silver cyanamide nanocrystals for the high-efficiency photocatalytic degradation of tetracycline†

Yulin Li, Chencong Cao, Qing Zhang, Ying Lu, Yanxi Zhao, Qin Li, Xianghong Li and Tao Huang *

Silver cyanamide (Ag_2NCN) is a type of functional semiconductor material with a visible-light response. Ag_2NCN nanocrystals with nanorod bundle-like (RB) or straw bundle-like (SB) assemblies were successfully prepared, and it was found that the as-prepared Ag_2NCN nanorod bundle (RB) samples had a narrower bandgap of 2.16 eV, which was lower than those reported. As a result, RB samples demonstrated a higher photocatalytic activity towards tetracycline (TC) degradation. The analyses of active species confirmed that both the photo-generated holes and $^{\bullet}O_2^-$ radicals of the RB sample played significant roles during the process of photocatalytic degradation of TC, and the holes were the main active species. These results indicated that effective charge separation could be achieved by adjusting the morphologies of Ag_2NCN nanocrystals. This study provides a new approach to prepare Ag_2NCN nanocrystals with a narrower bandgap and strong visible-light response towards antibiotic degradation.

Received 29th January 2021
Accepted 22nd February 2021

DOI: 10.1039/d1ra00770j

rsc.li/rsc-advances

Introduction

The environmental pollution and ecotoxicological effects caused by antibiotics have become one of the major environmental problems in China and even in the world. Antibiotics have been widely used in anti-infection therapy for humans and animals. Many antibiotics used in animal husbandry are difficult to be absorbed by animals, and about 30–90% of them are excreted directly into the environment in the form of prototypes or metabolites. Compared to the parent antibiotics, the toxicity of their metabolites and degradation products is greatly enhanced, although with lower activities. As one of the most important antibiotics, tetracycline (TC) is the most widely used in clinics. It is easy to accumulate in the water environment because of its good water solubility. It has been detected in aquatic environments such as surface water and groundwater as well as the inlets and outlets of sewage treatment plants.[1–3] After metabolism, most of TC is excreted in prototype into the environment, and it is difficult to degrade since it is nonbiodegradable.[4] TC antibiotic residues have a profound impact on the ecological environment and may eventually have harmful effects on human health and survival.[5–8] Therefore, it is imperative to develop efficient techniques to eliminate TC in the environment.

In recent years, photocatalytic degradation has received great interest on account of its unique advantages of high efficiency, low energy consumption, and environmental friendliness. Semiconductor photocatalysis has attracted great interest as a promising strategy for renewable energy generation and environmental remediation.[9–11] Under light irradiation, semiconductor photocatalytic materials can be activated by photons and can produce photo-generated electrons and holes, resulting in strong oxidation or reduction on their surfaces. However, the wider energy gap and the fast recombination of photogenerated electron–hole pairs greatly restrain the photocatalytic efficiency of the conventional semiconductor photocatalysts.[12–14] The environmentally friendly photocatalysts for TC degradation are of great significance for controlling antibiotic pollution. Up to now, although a series of semiconductor photocatalysts for TC degradation have been prepared,[15–18] it is still a challenge to explore novel high-efficiency visible-light responsive photocatalysts for antibiotic degradation.

Theoretically, silver cyanamide (Ag_2NCN) should demonstrate good visible-light response and high photocatalytic performance, and these properties have been confirmed by the previous reports.[19–22] In general, the 2p orbital energy levels of C and N atoms in Ag_2NCN are higher than those of O atoms in silver oxide, and the valence band energy level formed by the hybridization of the 2p orbitals of C and N atoms is further elevated. As a result, the bandgap for Ag_2NCN will become narrower under the premise that the band energy level remains

Key Laboratory of Catalysis and Energy Materials Chemistry of Ministry of Education, College of Chemistry and Materials Science, South-Central University for Nationalities, Wuhan 430074, China. E-mail: huangt208@163.com

† Electronic supplementary information (ESI) available: TEM, SEM, FT-IR, XRD, XPS, EDS, Mott–Schottky plots, UV-vis spectra, HPLC-MS and MALDI-TOF-MS. See DOI: 10.1039/d1ra00770j

unchanged compared with that of silver oxide. Simultaneously, the strong energy band dispersion effect facilitates to enhance the electron mobility, reduces the electron–hole recombination, and improves its photocatalytic conversion efficiency.

In addition, the electronic states of $[NCN]^{2-}$ in metal cyanamide are more delocalized than O $2p^6$ states in the metal oxide at both the maximum valence band and the minimum conduction band. In general, $[NCN]^{2-}$ can exist in the electronic form of symmetrical carbodiimide $[N{=}C{=}N]^{2-}$ (ref. 23–27) or asymmetrical cyanamide $[N{\equiv}C{-}N]^{2-}$. The inherent dipoles and dipolar fields of the asymmetrical $[N{\equiv}C{-}N]^{2-}$ (ref. 28–30) form in Ag_2NCN should promote photocatalytic activity by assisting the long-range migration of ions with opposite charges in the photochemical reactions. Therefore, Ag_2NCN has great potential application in solar-energy utilization and optoelectric fields. So far, however, the reports on the synthesis and photocatalytic performances of Ag_2NCN with different morphologies are still limited. In addition, silver cyanamide is mainly used in the degradation of dyes;[19,20] however, its application in the degradation of antibiotics has not been reported.

Herein, Ag_2NCN nanorod bundles as well as other nanostructures were synthesized with numerous amines as complexing agents by chemical deposition under nonaqueous conditions, and their photocatalytic activities towards the degradation of TC were investigated. The as-prepared Ag_2NCN nanorod bundles hold a direct bandgap (E_g) of 2.16 eV, which was lower than those reported and demonstrated high photocatalytic activity for TC degradation.

Experimental

Materials

Silver nitrate ($AgNO_3$), *N*,*N*-dimethylformamide (DMF), cyanamide (H_2NCN), *n*-octylamine, *t*-butylamine, tetracycline (TC), EDTA-2Na, benzoquinone (BQ), isopropanol (IPA), and all other chemicals were purchased from Sinopharm Chemical Reagent Co. Ltd. (Shanghai, China). All reagents were of analytical grade and used as received without further purification.

Syntheses of Ag_2NCN nanocrystals

In a typical synthesis, 0.17 g (1 mmol) of $AgNO_3$ was first dissolved in 3 mL of *N*,*N*-dimethylformamide (DMF). Then, 1 mL of *n*-octylamine was added. After stirring for 30 min, 1 mL of 1 mol L^{-1} H_2NCN solution in ethanol was injected at room temperature (25 °C), and the solution turned yellow immediately. After reaction for 30 min under constant stirring, 2 mL of acetone was added. Finally, the resultant suspension was centrifugated at 9000 rpm for 10 min, and the collected yellow precipitate was washed 3 times with DMF, acetone, and water. The obtained bright yellow product was dried in vacuum at 25 °C for 10 h.

Under the same conditions, Ag_2NCN nanocrystals were also synthesized using *t*-butylamine instead of *n*-octylamine.

Characterization

The phase analysis was conducted by X-ray diffraction (XRD) on a Bruker D8 Advance diffractometer employing Cu K_α irradiation with 40 kV and 50 mA. The observations of nanostructures and morphologies were conducted using a field-emission transmission electron microscope (STEM, Talos F200X G2) and a field-emission scanning electron microscope (SEM, SU8010), respectively. The elements of the samples were identified *via* energy dispersive X-ray spectroscopy (EDS), which was connected with STEM. The chemical composition was examined by X-ray photoelectron spectroscopy (XPS, VG Multilab 2000). The Brunauer–Emmett–Teller (BET) specific surface areas were determined through nitrogen adsorption isotherms at 373 K using a Micromeritics ASAP 2020 instrument and calculated from the linear part of the BET plot. FT-IR spectra were recorded on a Nexus-470 spectrometer. UV-vis diffuse reflection spectra (DRS) were measured on a spectrophotometer (Cary 5000).

Photoelectrochemical measurements

Transient amperometric *I*–*t* curve and electrochemical impedance spectroscopy (EIS) measurements were carried out on a CHI-660E electrochemical system with a three-electrode quartz cell under a LED (3 W) (Shenzhen LAMPLIC Science Co. Ltd., China). Saturated calomel electrode, platinum wire, and ITO coated with Ag_2NCN samples were used as the reference electrode, the counter electrode, and the working electrode, respectively. A 0.1 M Na_2SO_4 solution was used as the electrolyte.

Photocatalytic performance tests

The photocatalytic activities of the as-prepared Ag_2NCN nanocrystals were evaluated with tetracycline hydrochloride as the simulative pollutant under simulated sunlight irradiation. In a typical system, 50 mg of the as-prepared Ag_2NCN sample was ultrasonically dispersed into 50 mL of TC aqueous solution (10 mg L^{-1}) and then stirred for 30 min to reach the adsorption–desorption equilibrium in a dark box. A 300 W xenon lamp was used as the excitation light source. Perpetual circuit water was supplied to keep the system at room temperature. In the process of the photocatalytic reaction, 3 mL suspension was taken out with a syringe at constant time intervals and filtered using a 0.22 μm organic filter membrane. The resultant clear and transparent solution was measured using a UV-vis spectrophotometer. The cycling stability was also tested under the same condition. The relative active species during TC degradation were detected by trapping tests and electron spin resonance (ESR) on a JES FA-200 spectrometer. The intermediate products were analyzed by high performance liquid chromatography-mass spectrometry (HPLC-MS, Agilent LC-Q-TOF-MS 6520). The degradation products were detected using a matrix-assisted laser desorption ionization-time of a flight mass spectrometer (MALDI-TOF-MS, Bruker autoflex™ speed MALDI-TOF(TOF)).

Results and discussion

Characterization of Ag_2NCN nanocrystals

The representative morphologies of Ag_2NCN nanocrystals obtained with different amines as the capping agents are shown in

Fig. 1 and S1.† TEM images showed that the resulting Ag_2NCN nanocrystals in the *t*-butylamine system were present in straw-bundle-like architectures (straw bundles, donated as SB) assembled with numerous radical nanobelts with an average length of 1.1 μm (Fig. 1a), while rod bundles (RB) gathered with nanorods with an average length of 110 nm and a cross-section of 18 nm in the *n*-octylamine system (Fig. 1b). SEM images further confirmed their structural features (Fig. 1c and d).

The crystallographic structures of all the obtained samples were examined by XRD. It can be seen in Fig. 2a that the characteristic diffraction peaks for RB samples were obtained at 2θ values = 12.5, 19.4, 32.8, 37.9, 39.3, 41.0, and 52.1°, which can be well indexed to (100), (110), (202), (300), (220), (022), and (−322) lattice planes, corresponding to the monoclinic structure of Ag_2NCN according to the standard diffraction data (JCPDS no. 70-5232). The sharper diffraction peaks for RB, compared with those of SB samples (Fig. S2†) suggested its higher crystallinity.

The FT-IR spectra of RB showed strong absorption bands at 3451.49 and 1383.98 cm^{-1} wavenumbers (Fig. S3†), corresponding to N–H stretching vibration and in-plane bending vibration. The absorption bands at 2927.41 and 2857.38 cm^{-1} wavenumbers were indexed to C–H (CH_2 and CH_3) stretching vibrations. Moreover, the absorption bands at 2133.80, 1978.68, and 1511.09 cm^{-1} wavenumbers were identified as C≡N, NCN, and C–N stretching vibrations, revealing the existence of both symmetrical carbodiimide $[N{=}C{=}N]^{2-}$ and asymmetrical cyanamide $[N{\equiv}C{-}N]^{2-}$ electronic structures. In addition, the FT-IR data also indicated the existence of the ligand amine on the surface of Ag_2NCN nanocrystals.

The elemental compositions and chemical states of the as-prepared Ag_2NCN samples were measured by XPS. The results showed that the surface compositions consisted of four elements, namely C, N, Ag, and O (Fig. S4†). No other obvious impurity peak was observed, revealing a high purity. Among them, the characteristic peaks at 374.7 and 368.7 eV were observed for Ag 3d spectrum, corresponding to the binding energies of $3d_{3/2}$ and $3d_{5/2}$ of Ag^+ ions, as shown in Fig. 2b. It was noteworthy to mention that the Ag 3d peaks of RB shifted towards higher binding energies compared with SB, implying a deviation in the electron cloud of Ag^+ ion to other elements, which may be ascribed to different $[NCN]^{2-}$ structures.

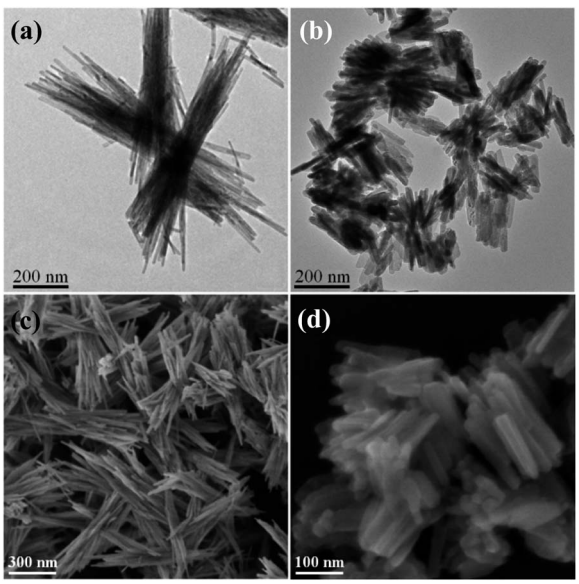

Fig. 1 (a and b) TEM and (c and d) SEM images of Ag_2NCN nanocrystals. (a) SB; (b) RB; (c) SB; (d) RB.

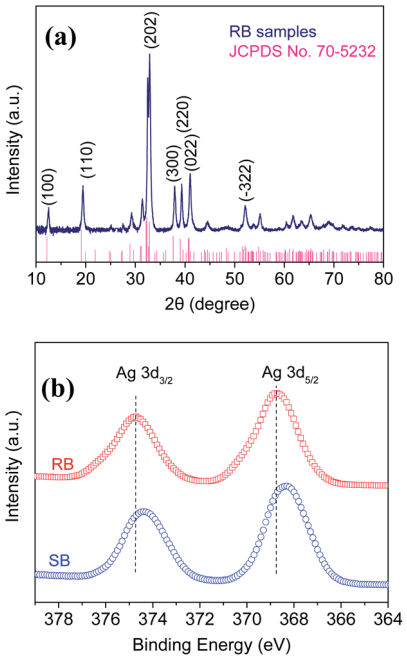

Fig. 2 (a) XRD patterns of RB samples. (b) XPS spectra of the Ag 3d region for RB samples.

The chemical compositions of the as-prepared Ag_2NCN samples were further determined by EDS. The EDS mapping and spot analyses for RB and SB as well as BP (prepared by the method in ref. 19) are shown in Fig. S5 and S6.† Compared with BP, it was found that the carbon contents in RB and SB were higher, which may be ascribed to the presence of ligand amines on the surface of the particles, as shown in the data listed in ESI.†

The formation mechanism of Ag_2NCN nanocrystals

To further understand the formation of Ag_2NCN nanocrystals, the effects of reaction temperature and time on the formation of RB and SB nanocrystals were investigated. Fig. S7 and S8† show the TEM images of Ag_2NCN nanocrystals prepared in *n*-octylamine and *t*-butylamine systems, respectively, at different temperatures. Compared with RB samples obtained at 25 °C (Fig. S7b†), no obvious difference either in length or in cross-section of the nanorod was observed for rod bundle-like nanostructures obtained at 0 °C (Fig. S7a†), while the same nanorod bundles were obtained at 60 °C and no obvious increase in the cross-section of the nanorod but an increased length was observed (Fig. S7c†). Similarly, no obvious change was observed for the straw bundle-like nanostructures obtained at different temperatures in the presence of *t*-butylamine except for the

length of the nanostraw bundles. Compared with SB samples obtained at 25 °C (Fig. S8b†), straw bundles with an average length of 550 or 2000 nm were produced at 0 or 60 °C (Fig. S8a and c†), respectively. Thus, it can be seen that straw bundle-like nanostructures cannot transform to rod bundle-like nanostructures. The experiment at a higher temperature was not conducted because of the reduction of silver ions.

Fig. S9† shows the TEM images of products obtained in the *t*-butylamine system at different reaction times. As the reaction time extended to 1 to 2 h, there was no significant change in the straw bundle-like nanostructures except for a little increase in aggregation. Therefore, by changing the temperature or prolonging the time, the nanostraw bundles cannot change to nanorod bundles. Similarly, no obvious change was observed for RB nanostructures by extending the reaction time.

Furthermore, it was found that the use of different amines has a significant effect on the morphology of Ag_2NCN nanocrystals. Instead of *n*-octylamine or *t*-butylamine, one of the other amines such as ethylamine, *n*-butylamine, or oleylamine were also introduced into the reaction systems. It can be seen in Fig. S10† that Ag_2NCN bulk nanocrystals were produced using ethylamine (Fig. S10a†), while Ag_2NCN rod-like nanocrystals were generated using *n*-butylamine (Fig. S10b†). Moreover, Ag_2NCN nanorods with less aggregation were formed when oleylamine was used (Fig. S10c†). These results implied that the increase in the carbon chain length of amines was beneficial to the formation of Ag_2NCN nanorods accompanied with less aggregation, while the branched chain structure was beneficial to the formation of long slender nanostructures. It can be seen that in the presence of *n*-octylamine Ag_2NCN nanorods were formed and assembled into rod bundles, which may be ascribed to fewer adsorptions of *n*-octylamine on the surface of nanorods. In the presence of *t*-butylamine, however, a significant number of thinner and longer straw-like nanostructures were generated and gathered into straw bundles due to a large number of adsorbed *t*-butylamine. Thus, the formation of nanorod bundles or nanostraw bundles was dependent upon the carbon chain length and structure of amines. Accordingly, the formation process of RB and SB samples can be illustrated as in the scheme (Fig. S11†).

DRS analyses and photoelectrochemical measurements

Furthermore, DRS was conducted to determine the bandgap of the as-prepared Ag_2NCN samples. As shown in Fig. 3a and b, the band gaps of RB and SB samples were estimated to be 2.16 and 2.24 eV, respectively, which were lower than those of the reported BP sample (2.30 eV).[19] The narrower bandgap of the RB sample implied a stronger visible-light response. These results showed that the effective charge separation could be achieved by adjusting the morphologies of Ag_2NCN nanocrystals.

The photo-induced electron–hole pair separation and transfer efficiency of RB and SB samples were investigated by transient amperometric *I*–*t* curves and EIS measurements. It can be seen in Fig. 3c that photocurrent responses under visible light irradiation could be observed over all the RB and SB samples as well as BP samples. Among them, the RB sample demonstrated not only an obviously enhanced photocurrent signal but also a slight increase during the light on–off cycling, whereas the photoresponse of the SB sample was relatively strong at the moment of light on and then decreased immediately. This may be attributed to the more electronic structure forms of asymmetrical cyanamide $[N{\equiv}C{-}N]^{2-}$ ions for the RB sample, in which the inherent dipoles and dipolar fields facilitate the long-distance migration of the opposite charge carries in optical activities, resulting in an increase in the effective charge migration. In addition, stronger electronic resonance existing in RB would be another reason for its enhanced photocurrent.

Moreover, EIS results displayed similar phenomena (Fig. 3d). Compared with SB and BP samples, the RB sample showed the lowest charge transport resistance and the highest charge transfer efficiency due to its smallest semicircle of the Nyquist plots. This result was consistent with the narrowest bandgap of the RB sample.

In order to investigate the properties of the as-prepared Ag_2NCN nanocrystals, the energy band structures were determined *via* Mott–Schottky plots by electrochemical tests. As shown in Fig. S12,† the positive slope of the curve indicated that either the RB sample (Fig. S12a†) or other samples (Fig. S12b†) were typical n-type semiconductors. For $C_{sc}{}^{2-} = 0$, the flat-band potential obtained by the extrapolating Mott–Schottky equation was approximately equal to the conduction band potential. The CB position of the RB sample was determined to be −0.59 V *versus* SCE. Combined with bandgap, the VB position of the RB sample was calculated to be +1.57 V *via* the empirical formula: $E_{VB} = E_{CB} + E_g$. The band structure diagram of RB is shown in Fig. S12c.† Similarly, the VB position of the SB sample was calculated to be 1.77 V, and the details are shown in ESI.†

BET analyses

In general, the photocatalytic activity is essentially dependent upon the separation efficiency of the photoinduced electron–hole pairs as well as the adsorption of antibiotic molecules in the photocatalytic degradation system. The BET specific surface areas of the RB and SB samples were investigated to characterize their adsorption abilities. Fig. 4a shows the nitrogen adsorption–desorption isotherms of RB and SB samples as well as that of the BP sample. It can be seen that a type H3 hysteresis loop for RB and SB samples suggested the type IV adsorption–desorption isotherm, which was different from that of BP. These distinctive characteristics may be ascribed to the layered assembly structures in RB and SB. The specific surface areas of RB and SB were measured to be 22.41 $m^2\ g^{-1}$ and 12.39 $m^2\ g^{-1}$, respectively, which are larger than that of the BP sample (1.2 $m^2\ g^{-1}$). Fig. 4b shows their relative pore size distribution, which demonstrated typical mesoporous characteristics. In addition, the biggest pore size of the RB sample implied that it was more beneficial for the adsorption of TC molecules.

Photocatalytic performances for TC degradation

The photocatalytic activities of the as-prepared Ag_2NCN nanocrystals with different morphologies were evaluated by the

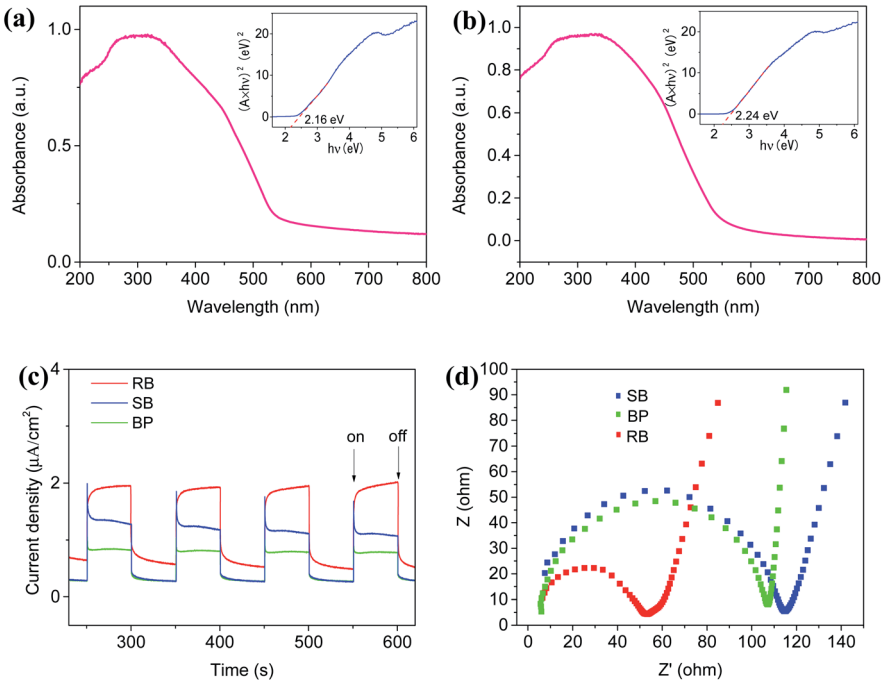

Fig. 3 (a) and (b) DRS spectra of RB and SB samples, respectively; (c) transient photocurrent response of the RB, SB, and BP samples irradiated under visible light; (d) EIS of the samples. The insets in (a) and (b) show the corresponding $(A \times h\nu)^2$–$h\nu$ curves.

degradation of TC under visible light. As shown in Fig. 5a, both RB and SB exhibited strong photocatalytic activity towards the degradation of TC. Compared with the SB sample, obviously, the RB sample demonstrated a higher photocatalytic performance since more than 96% of TC was removed within 120 min under the optimum conditions. Nevertheless, the degradation performance of the BP sample was close to that of the SB sample. Though the corresponding UV-vis absorption spectra showed that the main characteristic peak of TC at 357 nm gradually decreased with time for all the three samples (Fig. S13a†), the degree of degradation corresponding to the peak at 275 nm demonstrated significant differences, implying different degradation pathways. Moreover, the effects of other factors such as the catalyst dosage and pH value on the photocatalytic degradation process were also investigated. As shown in Fig. S14a,† the degradation of TC increased with the increase in the amount of RB. As the dosage of RB was 50 mg, the optimal degradation efficiency reached 96% in 120 min. Since Ag_2NCN nanocrystals would dissolve in a strongly acidic environment, the photocatalytic degradation of TC was carried out under a weak acidic condition. It can be seen that a weakly acidic aqueous solution was helpful for the degradation of TC in the first 40 min (Fig. S14b†). Fig. 5b shows the kinetic curves of TC degradation over different Ag_2NCN samples. A linear relationship between $\ln(C/C_0)$ and illumination time revealed a pseudo-first-order reaction for TC degradation. In addition, the pseudo-first-order rate constant K derived from the kinetic curve of the RB sample was the highest compared with other samples (Fig. 5c). These results indicated that the photocatalytic performance of the nanorod bundle-like Ag_2NCN nanocrystals was higher than that of the straw bundle-like Ag_2NCN assembly or BP sample, which may be attributed to the optimal charge separation–adsorption equilibrium in the RB sample. These results were coincident with their specific surface areas.

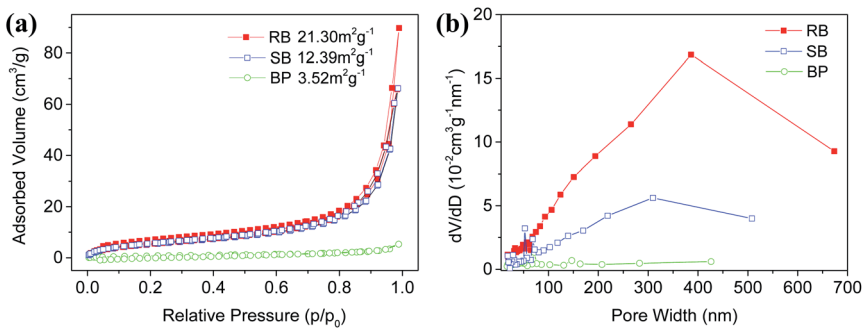

Fig. 4 (a) Nitrogen adsorption–desorption isotherms and (b) relative pore size distribution of RB, SB, and BP samples.

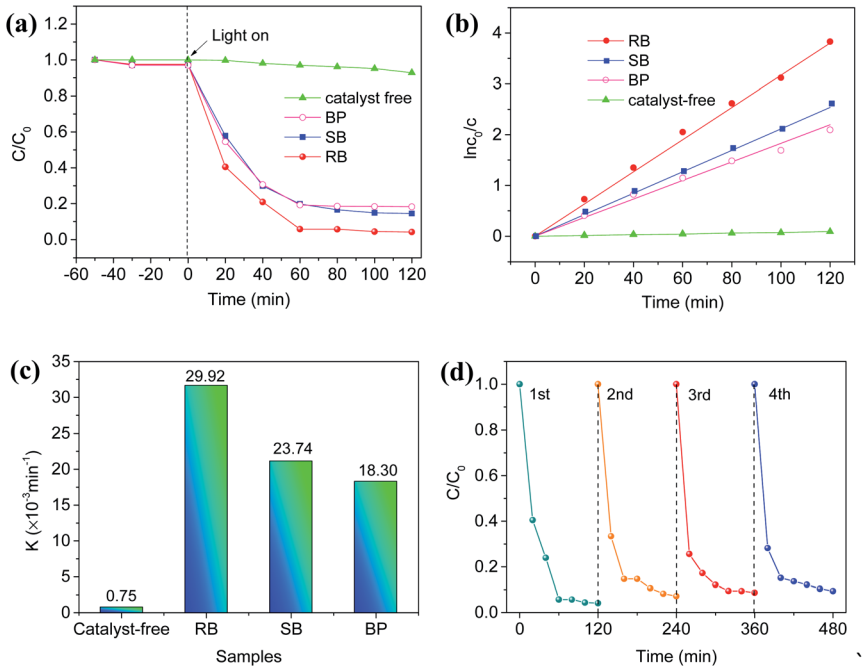

Fig. 5 (a) Photocatalytic degradation of TC over different samples (RB, SB, and BP) in 120 min (the optimum conditions: 50 mg of sample, 20 mg L^{-1} of TC solution, pH 9.62, 350 W of the light intensity); (b) the kinetic curves of TC degradation over different samples; (c) the apparent rate constants for TC degradation with different samples; (d) the cyclic degradations of TC over RB samples.

Furthermore, the cyclic degradation of TC was conducted to examine the stability of the catalyst. It can be seen in Fig. 5d that the degradation rate of TC over the RB sample showed a slight decline after four consecutive cycles, which may be ascribed to the loss of the collected catalyst. Compared with the original RB sample, no obvious variations were observed in XRD and XPS (Fig. S15†) as well as TEM measurements for RB after 4 cycles (Fig. S16†), indicating a strong structural stability of the RB sample in the process of photocatalytic degradation. SB samples showed the same catalytic stability in the photocatalytic degradation of TC. Their stability should be attributed to their aggregated bundle structures.

In order to further clarify the mechanism of the photocatalytic TC degradation, EDTA-2Na, benzoquinone (BQ), and isopropanol (IPA) were added into the RB-catalytic system to capture holes, $^{\bullet}O_2^-$ radicals, and $^{\bullet}OH$ radicals, respectively, under the same conditions. The kinetic curves and the degradation rates of the corresponding photocatalytic degradation process are shown in Fig. 6a and S17,† respectively. It can be seen that the photocatalytic degradation of TC was nearly inhibited completely under visible light in the system with EDTA-2Na. Besides, the degradation rate of TC decreased from 96% in 120 min without BQ to 66.7% in 120 min after adding BQ (Fig. S17†), while no obvious effect was observed with the addition of IPA. These results suggested that both the photogenerated holes and $^{\bullet}O_2^-$ radicals over the RB sample played significant roles during the photocatalytic degradation of TC, and the holes were the main active species. In addition, using dimethyl pyridine N-oxide (DMPO) as the trapping agent, ESR measurements showed typical characteristic peaks for DMPO-$^{\bullet}O_2^-$ adducts over the RB samples (Fig. 6b), which was consistent with trapping tests, confirming the existence of active oxygen species. Thus, $^{\bullet}O_2^-$ radicals were one of the active radicals for the effective photocatalytic degradation of TC.

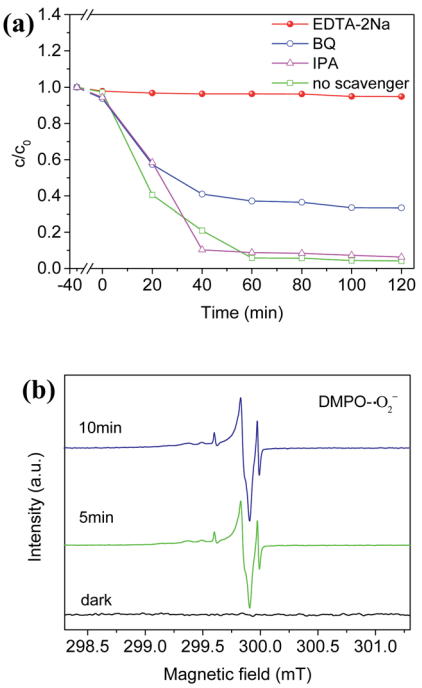

Fig. 6 (a) The photocatalytic activity of RB samples with different quenchers; (b) ESR spectra of DMPO-$^{\bullet}O_2^-$ adducts under light irradiation and in dark.

In addition, the intermediates produced in the process of photocatalytic degradation were analyzed *via* HPLC-MS and MALDI-TOF-MS, respectively. According to the HPLC-MS (Fig. S18†) and MALDI-TOF-MS (Fig. S19†) spectrograms, a possible pathway for the photocatalytic degradation of TC is provided in Fig. S20.† Under the attacks of $^{\bullet}O_2^-$ radicals and holes in the process of photocatalytic degradation, TC molecules were gradually oxidized and degraded to small molecule organics after a series of deamination, dealkylation, and ring-opening reactions.[15,31] Finally, these small molecule organics generated during the degradation process were mineralized into CO_2 and H_2O.

Conclusions

In summary, Ag_2NCN nanocrystals with nanorod bundle-like (RB) or straw bundle-like (SB) assemblies were successfully prepared using *n*-octylamine or *t*-butylamine, respectively, as the complexing agents by chemical deposition in DMF, and their photocatalytic activities for the degradation of TC were investigated. The results indicated that the effective charge separation could be achieved by adjusting the morphologies of Ag_2NCN nanocrystals. The as-prepared Ag_2NCN nanorod bundles (RB samples) demonstrated higher photocatalytic activity towards TC degradation due to the narrowest bandgap of the RB samples (2.16 eV) to date for Ag_2NCN semiconductors. The analyses of active species confirmed that both the photogenerated holes and $^{\bullet}O^{2-}$ had significant roles during the photocatalytic degradation of TC, and the holes were the main active species. This study will provide a promising functional material with a strong visible-light response for antibiotic degradation.

Conflicts of interest

There are no conflicts to declare.

Acknowledgements

Y. Li and C. Cao contributed equally to this work and should be regarded as co-first authors. This work was supported by the National Nature Science Foundation of China (Grant 21273289) and the Fundamental Research Funds for the Central Universities (CZZ20002).

Notes and references

1 M. Yousefi, S. Villar-Rodil, J. I. Paredes and A. Z. Moshfegh, Oxidized graphitic carbon nitride nanosheets as an effective adsorbent for organic dyes and tetracycline for water remediation, *J. Alloys Compd.*, 2019, **809**, 151783.

2 X. Zhou, J. Wang, C. Lu, Q. Liao, F. O. Gudda and W. Ling, Antibiotics in animal manure and manure-based fertilizers: occurrence and ecological risk assessment, *Chemosphere*, 2020, **255**, 127006.

3 K. Xu, J. Wang, H. Gong, Y. Li, L. Zhou and M. Yan, Occurrence of antibiotics and their associations with antibiotic resistance genes and bacterial communities in Guangdong coastal areas, *Ecotoxicol. Environ. Saf.*, 2019, **186**, 109796.

4 Z. Cetecioglu, B. Ince, M. Gros, S. Rodriguez-Mozaz, D. Barcel, D. Orhon and O. Ince, Chronic impact of tetracycline on the biodegradation of an organic substrate mixture under anaerobic conditions, *Water Res.*, 2013, **47**, 2959–2969.

5 S. Long, Y. Yang, S. G. Pavlostathis, F. Xiang, P. Sun, N. Li and L. Zhao, Toxicity of tetracycline and its transformation products to a phosphorus removing Shewanella strain, *Chemosphere*, 2020, **246**, 125681.

6 C. Q. Chen, L. Zheng, J. L. Zhou and H. Zhao, Persistence and risk of antibiotic residues and antibiotic resistance genes in major mariculture sites in Southeast China, *Sci. Total Environ.*, 2017, **580**, 1175–1184.

7 J. Sun, L. Jin, T. He, Z. Wei, X. Liu, L. Zhu and X. Li, Antibiotic resistance genes(ARGs) in agricultural soils from the Yangtze River Delta, China,, *Sci. Total Environ.*, 2020, **740**, 140001.

8 A. Booth, D. S. Aga and A. L. Wester, Retrospective analysis of the global antibiotic residues that exceed the predicted no effect concentration for antimicrobial resistance in various environmental matrices, *Environ. Int.*, 2020, **141**, 105796.

9 H. Dong, X. Zhang, J. Li, P. Zhou, S. Yu, N. Song, C. Liu, G. Che and C. Liu, Construction of morphology-controlled nonmetal 2D/3D homojunction towards enhancing photocatalytic activity and mechanism insight, *Appl. Catal., B*, 2020, **263**, 118270.

10 H. Hu, Y. Lin and Y. H. Hu, Core-shell structured TiO_2 as highly efficient visible light photocatalyst for dye degradation, *Catal. Today*, 2020, **341**, 90–95.

11 Y. Ma, Y. Xu, X. Ji, M. Xie, D. Jiang, J. Yan, Z. Song, H. Xu and H. Li, Construction of polythiophene/$Bi_4O_5I_2$ nanocomposites to promote photocatalytic degradation of bisphenol A, *J. Alloys Compd.*, 2020, **823**, 153773.

12 H. G. Kim, D. W. Hwang and J. S. Lee, An undoped, single-phase oxide photocatalyst working under visible light, *J. Am. Chem. Soc.*, 2004, **29**, 8912–8913.

13 C. A. Roberts, S. P. Phivilay and I. E. Wachs, Nature of surface oxygen intermediates on TiO_2 during photocatalytic splitting of water, *Chin. Chem. Lett.*, 2018, **29**, 769–772.

14 S. Misra, L. Li, D. Zhang, J. Jian, Z. Qi, M. Fan, H.-T. Chen, X. Zhang and H. Wang, Self-assembled ordered three-phase Au-$BaTiO_3$-ZnO vertically aligned nanocomposites achieved by a templating method, *Adv. Mater.*, 2019, **31**, 1806529.

15 S. Li and J. Hu, Photolytic and photocatalytic degradation of tetracycline: Effect of humic acid on degradation kinetics and mechanisms, *J. Hazard. Mater.*, 2016, **318**, 134–144.

16 T. Soltani, A. Tayyebi and B.-K. Lee, Photolysis and photocatalysis of tetracycline by sonochemically heterojunctioned $BiVO_4$/reduced graphene oxide under visible-light irradiation, *J. Environ. Manage.*, 2019, **232**, 713–721.

17 F. Chen, Q. Yang, J. Sun, F. Yao, S. Wang, Y. Wang, X. Wang, X. Li, C. Niu, D. Wang and G. Zeng, Enhanced photocatalytic degradation of tetracycline by AgI/$BiVO_4$ heterojunction

under visible-light irradiation: mineralization efficiency and mechanism, *ACS Appl. Mater. Interfaces*, 2016, **48**, 32887–32900.

18 W. Jiang, Z. Li, C. Liu, D. Wang, G. Yan, B. Liu and G. Che, Enhanced visible-light-induced photocatalytic degradation of tetracycline using BiOI/MIL-125(Ti) composite photocatalyst, *J. Alloys Compd.*, 2021, **854**, 157166.

19 W. Zhao, Y. Liu, J. Liu, P. Chen, I.-W. Chen and F. Huang, Controllable synthesis of silver cyanamide as a new semiconductor photocatalyst under visible-light irradiation, *J. Mater. Chem. A*, 2013, **1**, 7942–7948.

20 B. Jia, W. Zhao, L. Fan, G. Yin, Y. Cheng and F. Huang, Silver cyanamide nanoparticles decorated ultrathin graphitic carbon nitride nanosheets for enhanced visible-light-driven photocatalysis, *Catal. Sci. Technol.*, 2018, **8**, 1447–1453.

21 W. Zhao, J. Pan and F. Huang, Nonaqueous synthesis of metal cyanamide semiconductor nanocrystals for photocatalytic water oxidation, *Chem. Commun.*, 2018, **13**, 1575–1578.

22 H. Meng, X. Li, X. Zhang, Y. Liu, Y. Xu, Y. Han and J. Xu, Fabrication of nanocomposites composed of silver cyanamide and titania for improved photocatalytic hydrogen generation, *Dalton Trans.*, 2015, **46**, 19948–19955.

23 X. Liu, M. Krott, P. Müller, C. Hu, H. Lueken and R. Dronskowski, Synthesis, Crystal structure, and properties of MnNCN, the first carbodiimide of a magnetic transition metal, *Inorg. Chem.*, 2005, **44**, 3001–3003.

24 X. Liu, R. Dronskowski, R. K. Kremer, M. Ahrens, C. H. Lee and M. Whangbo, Characterization of the magnetic and structural properties of copper carbodiimide, CuNCN, by neutron diffraction and first-principles evaluations of its spin exchange interactions, *J. Phys. Chem. C*, 2008, **112**, 11013–11017.

25 X. Liu, L. Stork, M. Speldrich, H. Lueken and R. Dronskowski, FeNCN and $Fe(NCNH)_2$: synthesis, structure, and magnetic properties of a nitrogen-based pseudo-oxide and -hydroxide of divalent iron, *Chem.–Eur. J.*, 2009, **15**, 1558–1561.

26 M. Krott, X. H. Liu, B. P. T. Fokwa, M. Speldrich, H. Lueken and R. Dronskowski, Synthesis, crystal-structure determination and magnetic properties of two new transition-metal carbodiimides: CoNCN and NiNCN, *Inorg. Chem.*, 2007, **46**, 2204–2207.

27 M. G. Down, M. J. Haley, P. Hubberstey, R. J. Pulham and A. E. Thunder, Synthesis of the dilithium salt of cyanamide in liquid lithium; X-ray crystal structure of Li_2NCN, *J. Chem. Soc., Chem. Commun.*, 1978, **21**, 52–53.

28 W. P. Liao, C. H. Hu, R. K. Kremer and R. Dronskowski, Copper-, cobalt-, and manganese-containing 17-tungsto-2-germanates, *Inorg. Chem.*, 2004, **43**, 5884–5890.

29 M. Becker, J. Nuss and M. Jansen, Crystal structure and spectroscopic data of silver cyanamide (in German), *Z. Naturforsch., B: J. Chem. Sci.*, 2000, **55B**, 383–385.

30 R. Cao and K. Tatsumi, Use of dipotassium cyanamide for the synthesis of cyanoimido (NCN^{2-}) complexes of tungsten and cobalt, *Chem. Commun.*, 2002, **18**, 2144–2145.

31 Z. Chen, C. Huang, T. Zhou and J. Hu, Strike a balance between adsorption and catalysis Capabilities in $Bi_2Se_{3-x}O_x$ composites for high-efficiency antibiotics remediation, *Chem. Eng. J.*, 2020, **382**, 122877.